PAPER

Check for updates

Molybdenum-doped iron oxide nanostructures synthesized *via* a chemical co-precipitation route for efficient dye degradation and antimicrobial performance: *in silico* molecular docking studies†

Tahira Shujah,[a] Anum Shahzadi,[b] Ali Haider, [ID][c] Muhammad Mustajab, [ID][a] Afsah Mobeen Haider,[a] Anwar Ul-Hamid, [ID][de] Junaid Haider,[f] Walid Nabgan [ID] *[g] and Muhammad Ikram [ID] *[a]

In this research, various concentrations of molybdenum (2, 4 and 6 wt%) doped Fe_3O_4 nanostructures (Mo-Fe_3O_4 NSs) were prepared *via* a co-precipitation technique. Various techniques were then used to investigate the optical, morphological and structural properties of the NSs in the presence of the dopant materials. X-ray diffraction (XRD) was used to investigate the crystalline nature of the prepared NSs and confirm the orthorhombic and tetragonal structure of Fe_3O_4, with a decrease in crystallinity and crystallite sizes of 36.11, 38.45, 25.74 and 24.38 nm with increasing concentration of Mo (2, 4 and 6%). Fourier-transform infrared (FTIR) spectroscopy analysis was carried out to examine the functional groups in the NSs. Structure, surface morphology and topography were examined *via* field emission scanning electron microscopy (FE-SEM) and transmission electron microscopy (TEM), which confirmed the fabrication of nanoparticles and nanorods and a floccule-like morphology with a higher doping concentration and the interlayer *d*-spacing was calculated using high-resolution (HR)TEM, the results of which were a good match to the XRD data. The presence of Mo, Fe and O in a lattice of Mo (2, 4 and 6%) doped Fe_3O_4 was confirmed by energy dispersive X-ray spectroscopy (EDS) analysis. The energy band gap (E_g) was measured *via* the optical analysis of pure and doped samples, showing a decrease from 2.76 to 2.64 eV. The photoluminescence (PL) spectra exhibit a higher charge combination rate of electron−hole pairs with a higher concentration of doping. The NSs exhibited excellent catalytic activity (CA) in degrading methylene blue (MB) dye in a basic medium by around 86.25%. Additionally, the antimicrobial activity was tested against *Escherichia coli* (*E. coli*) bacteria. Pairs of electrons and holes are the fundamental basis for generating reactive oxygen species that kill bacteria. The significant inhibition zones were calculated against *E. coli* bacteria at around 3.45 mm compared to ciprofloxacin. *In silico* docking investigations of the Mo-Fe_3O_4 NSs for dihydropteroate synthase (DHPS, binding score: 6.16 kcal mol^{-1}), dihydrofolate reductase (DHFR, binding score: 6.01 kcal mol^{-1}), and β-ketoacyl-acyl carrier protein synthase III (FabH, binding score: 5.75 kcal mol^{-1}) of *E. coli* show the suppression of the aforementioned enzymes as a potential mechanism besides their microbicidal assay.

1 Introduction

Environmental pollution, caused by rapid urbanization and industrialization, has a significantly impact on human lives. On a regular basis, an enormous amount of non-biodegradable as well as carcinogenic colored dyes are discarded in freshwater resources from the textile, rubber, food, plastic, leather, paper and cosmetics industries, where these toxic organic dyes are the waste materials of industrial processes.[1–3] Heavy metals ions and inorganic compounds such as mineral acids, trace

[a]*Department of Physics, University of Central Punjab, Lahore, 54000, Punjab, Pakistan. E-mail: dr.muhammadikram@gcu.edu.pk*

[b]*Faculty of Pharmacy, The University of Lahore, Lahore, Pakistan*

[c]*Department of Clinical Medicine, Faculty of Veterinary and Animal Sciences, Muhammad Nawaz Shareef, University of Agriculture, Multan, Punjab, 66000, Pakistan*

[d]*Solar Cell Applications Research Lab, Department of Physics, Government College University Lahore, Lahore, Punjab, Pakistan*

[e]*Core Research Facilities, King Fahd University of Petroleum & Minerals, Dhahran, 31261, Saudi Arabia*

[f]*Tianjin Institute of Industrial Biotechnology, Chinese Academy of Sciences, Tianjin 300308, China*

[g]*Departament d'Enginyeria Química, Universitat Rovira i Virgili, 43007 Tarragona, Spain. E-mail: walid.nabgan@urv.cat*

† Electronic supplementary information (ESI) available. See DOI: https://doi.org/10.1039/d2ra07238f

elements, inorganic salts, sulphates and metal complexes *etc.*, as well as organic constituents, have been found in industrial wastewater in the form of pesticides, polyaromatic hydrocarbons, dyes and phenols, *etc.*, as hazardous pollutants.[4,5] Different types of dyes used in industries and found in wastewater, such as methylene blue (MB), phenothiazine, methylene orange, rhodamine B, azo, and triphenylmethane dyes, pose a serious environmental threat to living human beings due to their potential carcinogenicity and toxicity.[6] MB is a cationic (positively charged) organic dye that contributes to many health issues and water contamination,[7] but has widespread application across various industries, including the textile, veterinary and pharmaceuticals industries.[8,9] MB has several negative effects on human health, such as nausea, vomiting, breathing difficulties and gastritis problems.[10] Water must therefore be cleaned in order to sustain life on Earth, which is a major research bottleneck. In this regard, multiple techniques have manifested for water purification, including catalysis and photocatalysis activities, ultrafiltration, co-precipitation, desalination and reverse osmosis for dye degradation.[11–13] Environmental waste is released from industries, which needs to be converted into an acceptable form before its disposal into freshwater resources.[14] Waste recovery processes have been utilized to treat water cost-effectively and sustainably.[15] A constructed wetland for sewage treatment method has found widespread use worldwide. The designed wetland system for domestic sewage treatment risks polluting groundwater and surface water to evaluate its long-term effectiveness.[16,17] Catalysis, ion exchange, photocatalysis, electrolysis, chemical precipitation, carbon filtering, reverse osmosis, microbial control adsorption and nanofiltration are a few of the most commonly used techniques for removing pollutants from industrial wastewater.[3,18–20] Among the discussed methods, catalysis is the most attractive method because of its cost, ecological, and energy-efficient benefits.[21]

In the dairy sector, mastitis is one of the most common diseases, leading to financial damage and a reduction in milk production worldwide. Mastitis is associated with physical alterations in the chemistry of milk and pathological variations in the mammary gland system. Microorganisms, including fungi, viruses and bacteria, cause several diseases, one of which is mastitis. The most common multidrug resistance (MDR) bacteria are *Escherichia coli* (*E. coli*) and *Staphylococcus aureus* (*S. aureus*).[22,23] *S. aureus* is the most common Gram-positive bacterium that causes nosocomial infections in hospitals and other healthcare facilities worldwide.[24,25] *E. coli* bacteria are Gram-negative and a well-established bioindicator of contaminated food and water, and its presence can lead to diarrhea and in some cases, generate hemolytic uremic syndrome.[26,27] In recent decades, new species of numerous drug-resistant bacteria, such as Gram-positive (*S. aureus*) and Gram-negative (*E. coli*) bacteria, have been discovered and developed, which pose a significant risk to human health.[28]

Metal oxides (MOs) have been used in large quantities for degrading organic impurities and killing pathogenic hazardous bacteria in industrial wastewater. Nanosized metallic oxides have a wide variety of applications in industry and technology,

some of which include optical and mechanical components, as well as environmental and optical components.[29] Transition and rare metal oxides, such as CeO_2, MnO_2, TiO_2, SnO_2, Fe_3O_4 and CaO_2, have been considered to be promising for water purification, hydrogen generation and sterilization.[30,31] Among these, Fe_3O_4, with a narrow band gap and high surface area, is one of the most common n-type semiconductor materials that has important optoelectrical and chemical applications due to its numerous characteristics such as efficiency and economy, environmental friendliness, inertness to chemical changes, and great biocompatibility.[32] The combination of metal and MOs improves the recombination of photogenerated electrons and holes and also limits the utilization of MOs in photocatalytic applications.[33–35] $Mo-Fe_2O_3$ acts as an electron mediator, capturing produced electrons and assisting in the proper utilization of electron conductivity.

The aim of this research work was to examine the efficient dye degradation and antimicrobial performance of $Mo-Fe_3O_4$ NSs synthesized *via* a co-precipitation method, with the prepared samples used to remove organic and inorganic pollutants from wastewater through catalytic reduction. Moreover, the optical, morphological and structural properties of Fe_3O_4 and Mo-doped Fe_3O_4 were analyzed using X-ray diffractometry (XRD), Fourier-transform infrared (FTIR) spectroscopy, selected area electron diffraction (SAED), scanning electron microscopy (SEM), transmission electron microscopy (TEM), energy-dispersive X-ray spectroscopy (EDS), mapping, ultraviolet-visible (UV-vis) and photoluminescence (PL) spectroscopies, and anti-microbial experiments against *E. coli* (Gram-negative) bacteria. Using computational methods, the hidden mechanisms underlying a wide range of biological processes can be examined. Here, we assessed the affinity of $Mo-Fe_3O_4$ NSs for the *E. coli* DHFR, DHPS, and FabH enzymes, and molecular docking predictions were carried out to learn about the binding propensity of the nanocomposite.

2 Experimental section

2.1 Materials

Iron nitrate nonahydrate (Fe $(NO_3)_3 \cdot 9H_2O$, 98%), sodium hydroxide (NaOH, 98%), and ammonium molybdate $((NH_4)_6 \cdot Mo_7O_{24}$, 99%) were acquired from Sigma-Aldrich, Germany. In this investigation, only chemicals of an analytical grade were utilized; therefore, there was no need for additional purification in any form.

2.2 Synthesis of Fe_3O_4 and Mo-doped iron oxide nanostructures

A solution of 0.5 M of $Fe(NO_3)_3 \cdot 9H_2O$ was used to synthesize Fe_3O_4 nanostructures *via* a chemical co-precipitation route with continuous stirring and heating at 100 °C for 1 h. 0.5 M of NaOH solution was added dropwise to maintain the pH at around 12 and to form a precipitate under constant stirring and heating at 90 °C for 2 h. The precipitate was scrubbed multiple times using deionized water (DIW) by centrifugation at 7000 rpm to remove impurities. The precipitate was dried for 12 h at 120 °C and then
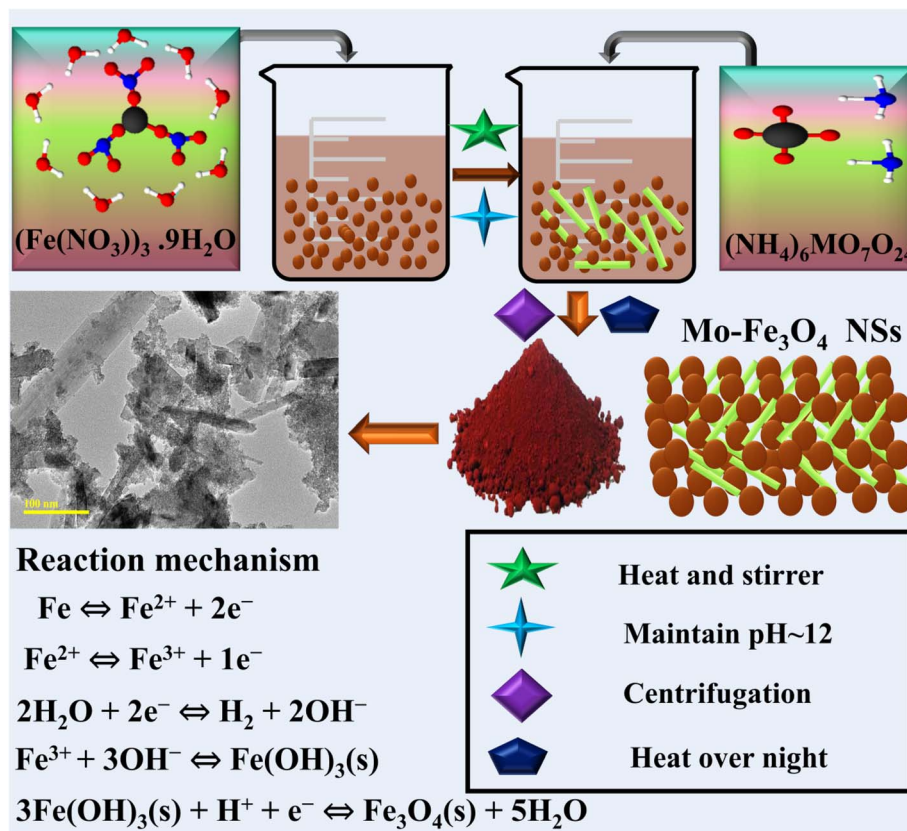
Reaction mechanism

$Fe \Leftrightarrow Fe^{2+} + 2e^-$

$Fe^{2+} \Leftrightarrow Fe^{3+} + 1e^-$

$2H_2O + 2e^- \Leftrightarrow H_2 + 2OH^-$

$Fe^{3+} + 3OH^- \Leftrightarrow Fe(OH)_3(s)$

$3Fe(OH)_3(s) + H^+ + e^- \Leftrightarrow Fe_3O_4(s) + 5H_2O$

Fig. 1 Schematic representation and description of the synthesized Fe_3O_4 and Mo-Fe_3O_4 nanostructures.

ground into a powder. In order to synthesize Mo-doped Fe_3O_4 samples with varying concentrations of Mo (2, 4 and 6%), the above-described method was chosen as the fabrication method. A schematic representation of the preparation method and reaction mechanism are shown in Fig. 1.

2.3 Catalytic activity (CA)

MB acts as an oxidizing agent and was used to evaluate the catalytic potential of bare and Mo-doped Fe_3O_4 NSs in the presence of the reducing agent sodium borohydride (NaBH$_4$), with the synthesized NSs acting as a catalyst. All reagents, including MB and NaBH$_4$, were prepared freshly to make ensure the validity of the results. First, 3 ml of an aqueous solution of MB was combined with 400 ml of freshly prepared NaBH$_4$ solution and combined with 400 ml of pure and Mo (2, 4 and 6%) doped Fe_3O_4 NSs. A catalyst is used to reduce the surface energy of reaction activation, improving the stability and reaction rate. Adsorption occurs in the presence of NaBH$_4$ when the catalyst is added to MB solution. Calculating the reaction rates was achieved by monitoring the decolorization of the solution as well as changes in the absorption maximum of the dye over time. Even though particles of smaller size have a higher ratio of surface area to total volume, which leads to increased CA, the dimensions of the nanoparticles affect the CA of the MB dye. The most common type of redox indicator MB used as reductant

in analytical chemistry, and blue during oxidation and decolorized in reduced form as revealed in Fig. S1.†

2.4 Isolation and identification of MDR *E. coli*

2.4.1 Isolation of *E. coli*

2.4.1.1 Sample collection. Immediate milking into sterile glass containers was employed to accumulate unpasteurized milk specimens from lactating dairy cows from various markets, veterinarian clinics, and farmlands in Punjab, Pakistan. Raw milk samples were delivered to the lab at 4 °C instantaneously after being collected. MacConkey agar was used to enumerate the coliform bacteria in the unpasteurized milk. Each plate was incubated for 48 h at 37 °C.

2.4.2 Identification and characterization of bacterial isolates.
The preliminary identification of *E. coli* was predicated on Gram stain colonial morphology and numerous biochemical tests compared to Bergey's Manual of Determinative Bacteriology.[36]

2.4.2.1 Antibiotic susceptibility. The disc diffusion technique was used to test antibiotic susceptibility[37] on Mueller Hinton agar (MHA). Experiments were carried out to determine the extent to which *E. coli* had developed resistance to 5 μg of the antibiotic ciprofloxacin (Cip).[38] A turbidity level of 0.5, according to the MacFarland standard, was achieved through the cultivation of purified cultures of *E. coli*. After that, the bacteria were dispersed on Muller Hinton Agar (MHA) (Oxoid Limited,

Basingstoke, UK), and antibiotic discs were positioned at a distance on the inoculated plate surface. This was carried out to avoid the interruption of zones of inhibition. The plates were cultured for 48 h at 37 °C, and the data were analyzed in a manner consistent with the suggestions made available by the Diagnostic, Therapeutic, and Laboratory Standard Institute.[39] MDR bacteria were found to be resistant to at least three antibiotics.[40]

2.4.2.2 Antimicrobial activity. To measure the *in vitro* antimicrobial action potential, the agar well diffusion method was applied to assess the antimicrobial properties of Fe_3O_4 and Mo (2, 4 and 6%) doped Fe_3O_4 by measuring the inhibition zones against MDR *E. coli*. Agar plates were inoculated with MDR *E. coli* at a concentration of 1.5×10^8 CFU per ml (0.5 McFarland standard) on MacConkey agar. *E. coli* pathogens were recovered efficaciously from ovine mastitis fluid to assess the bactericidal functionality of pristine and doped nanostructures. The pathogenic bacteria remedies were scrubbed on agar plates and 6 mm boreholes in diameter were generated with a sterile cork borer. Ciprofloxacin is a conventional drug (5 μg/50 ml) used as a positive control and 50 μl of DIW served as negative control, and the boreholes were filled with host and the doped nanostructure at high and low concentrations (1.0 mg/50 μl) and (0.5 mg/50 μl), respectively. Afterwards, the plates were incubated at room temperature overnight and inhibited zones around the wells were measured using a Vernier caliper. The antimicrobial action of the synthesized samples was determined by measuring the diameters (mm) of the inhibition zones that surrounded the wells.[41]

2.4.2.3 Statistical analysis. The anti-microbial efficiency was measured by the zones of inhibition measurement size (mm), and the diameters of the inhibition zones were subjected to statistical examination using one-way analysis of variance (ANOVA) in SPSS 20.[22]

2.5 Molecular docking studies

In silico docking, a promising approach for identifying the distinguishing structural features underlying microbicidal efficacy, was employed to anticipate the putative mechanism for the Mo-Fe_3O_4 NSs. The pivotal enzymes for folate biogenesis, dihydrofolate reductase (DHFR) and dihydropteroate synthase (DHPS), as well as the -ketoacyl-acyl carrier protein synthase III (FabH) of fatty acid synthesis, have been identified as intriguing targets for antibiotic discovery. The 3D structural features of the specified enzymes were acquired from the Protein Data Bank and generated *via* a protein production tool for docking of Mo-Fe_3O_4 NSs into the active region. Annexation codes for the preferred targets were set as: 2ANQ ($DHFR_{E.\ coli}$),[42] 5U0V ($DHPS_{E.\ coli}$)[43] and 4Z8D ($FabH_{E.\ coli}$).[44] The docking inquiry was conducted using the SYBYL-X 2.0 software. Similar to our earlier study, SYBYL-X 2.0 was employed to create 3D structures of the compounds and analyze nanoparticle binding affinities using active site residues of the chosen proteins.[45,46]

3 Results and discussion

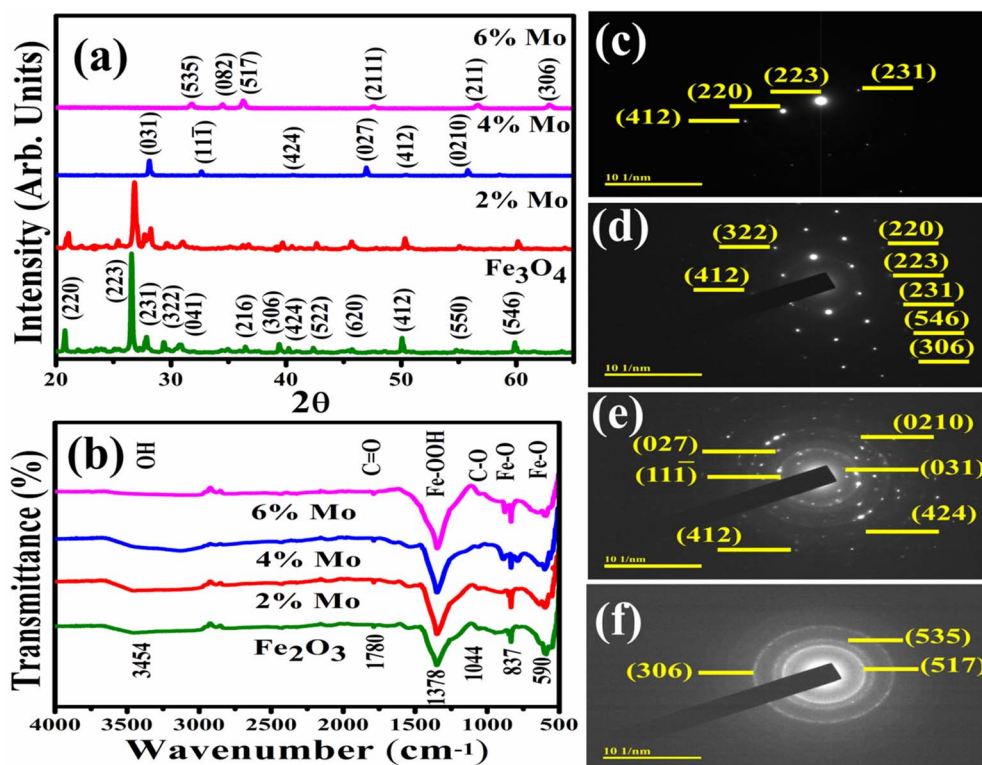The crystallographic structures, phase purities, chemical compositions and complex interplanar characteristics of the

Fig. 2 (a) XRD diffraction patterns, (b) FTIR spectra, and (c–f) SAED patterns of Fe_3O_4 and Fe_3O_4 doped with various amounts of Mo.

samples were identified by XRD in the range of $2\theta = 20$–$65°$ and the corresponding results are presented in Fig. 2a. Sharp diffraction peaks with relevant planes for pristine and Mo (2%) doped Fe_3O_4 at 2θ angles were observed at 20.7° (220), 26.6° (223), 27.7° (231), 29.2° (322), 30.6° (041), 36.33° (216), 39.4° (306), 40.2° (424), 42.3° (522), 45.7 (620), 50.1° (412), 54.7° (550) and 59.8° (546), revealing that the orthorhombic and tetragonal structures matched well with the standard JCPDS 01-076-0958 and 01-076-0956, and 03-065-0390 cards with space group $Pmc2_1$, $Pmca$ and $P4_12_12$, respectively. The 2% Mo doped sample showed a peak oriented at 26.6° with decreased intensity, corresponding to the (223) plane, with its orthorhombic structure matching JCPDS 01-076-0958. The 4% Mo-doped Fe_3O_4 sample showed additional peaks at 28.3, 32.4°, 47° and 55.8°, ascribed to (031), (111), (027) and (0210) planes, exhibiting that the hexagonal and monoclinic structures of Fe_2O_3 matched with JCPDS card numbers 01-076-1821 and 00-016-0653. The 6% Mo-doped Fe_3O_4 showed peaks at 31.9 (535), 34.4 (082), 36.2 (517), 47.5 (2111), 56.4 (211), and 62.7 (306), revealing the orthorhombic and rhombohedral structure of FeO and Fe_2O_3 could be well matched to the JCPDS card numbers 01-071-0161 and 01-084-0308 in the space groups $Abm2$ and $R\bar{3}C$, respectively. Upon doping, slight peak shifts with a significant decrease in peak intensity were manifested due to the enhanced structural disorder and amorphous nature of the high concentration of flocules on the Mo-doped samples.[47]

The crystallite size (*D*) of the prepared materials was measured using the Debye–Scherrer equation. The measured values of the crystallite sizes were 36.11, 38.45, 25.74, and 24.38 nm, with peak positions at 2θ angles of 26.6, 26.6, 28.3 and 36.26 °corresponding to the (223), (223), (031) and (517) planes of pure and Mo (2, 4 and 6%) doped Fe_3O_4, respectively. The difference in crystalline size basically depends on the angles of diffraction and the effect of peak broadening. The measured results indicate that the crystalline size first increases with the incorporation of the dopant and then decreases with increasing concentration. The dislocation density (*δ*) was measured using the equation $\delta = 1/D^2$, where *D* is the crystalline size. The increase in dislocation density with decreasing crystalline size was measured as 0.000767, 0.000676, 0.001509 and 0.001682 for pristine and Mo (2, 4 and 6%), respectively. The micro-strains (*ε*) of the prepared samples were calculated using the Williamson and Smallman equation $\varepsilon = \beta/4\tan\theta$. The micro-strains were calculated and found to be 0.002061, 0.001909, 0.002695 and 0.002131 for Fe_3O_4 and Mo-Fe_3O_4 at various concentrations (2, 4 and 6%), respectively.

FTIR spectroscopy was employed to determine the nature of the functional groups on the surface of NSs in the range of 4000–400 cm^{-1}, with the results shown in Fig. 2b. Transmittance peaks were detected at wavenumbers of 590, 837, 1044, 1348, 1780, and 3454 cm^{-1}. The transmittance bands are governed by the crystalline structure and chemical composition of the material. The spectra of Fe_3O_4 and Mo-doped Fe_3O_4 coexist and display strong bands at 590 and 837 cm^{-1}, ascribed to Fe–O vibrations.[48,49] The absorption band observed at 1348 cm^{-1} has been reported for ferrihydrite.[49,50] The peak observed at 1780 cm^{-1} is associated with the carbonyl group C=O.[51] The

band at 1044 cm^{-1} has been associated with the C–O group.[52] The band at 3454 cm^{-1} was attributed to the stretching vibration of the hydroxyl group, which originated from exposure of the sample to the moist atmospheric environment.[53] SAED analysis was used to indicate the crystalline structure of the host and Mo doped at various concentrations (2, 4 and 6%) in the NSs, as indicated in Fig. 2c–f. The pristine and 2% Mo-doped Fe_3O_4 sample are single-crystalline in nature (Fig. 2d), while the 4% Mo-doped sample is polycrystalline in nature, as can be seen from the concentric ring and the 6% doped sample is semicrystalline in nature, as shown in Fig. 2e and f. These discussed planes of NSs can be matched to the XRD results and satisfy the Bragg diffraction conditions.

The surface morphologies of pristine Fe_3O_4 and the (2, 4 and 6%) Mo-doped Fe_3O_4 were analyzed by FE-SEM, as shown in Fig. S2(a–d)†, where the black spot shows the absence of the sample. The FE-SEM results exhibit the evolution of the nanoparticles of Fe_3O_4, while at the same time, the morphologies of the (2, 4 and 6%) Mo-doped Fe_3O_4 nanorods are shown in Fig. S2(b and c)†. The bare Fe_3O_4 particles have a heterogeneous surface and are quasi-spherical in shape. Furthermore, the images reveal that the particles exhibit slight aggregation due to the magnetic dipole moment between the particles.[54] Increasing the concentration of Mo (2, 4 and 6%), the agglomeration increased and surface floccules of Mo on the surface of Fe_3O_4 formed and increased in number, as shown in Fig. S2(d).†

TEM analysis was used to reveal the detailed morphological information about the synthesized Fe_3O_4 and (2, 4 and 6%) Mo-doped Fe_3O_4 NSs, as shown in Fig. 3a–d. Pristine Fe_3O_4 exhibits the formation of uniformly distributed spherical-shaped nanoparticles. The addition of Mo showed that the morphology changed into an agglomerated form, with the self-aggregation of nanorods and nanoparticles. Increasing the concentration of Mo (2, 4 and 6%) gradually led to a decrease in the crystalline nature and formation of the nanorods, as presented in Fig. 3b and c. Subsequently, the 6% Mo-doped Fe_3O_4 sample exhibited a completely different morphology, where the nanorods disappeared and an excess of surface floccules of Mo emerged on the surface of the nanoparticles,[47] as presented in Fig. 3d.

HRTEM was used to measure the interlayer d-spacing using Gatan software of the synthesized Fe_3O_4 and various concentrations of 2, 4 and 6% Mo-doped NSs as indicated in Fig. S3(a–d)†. The calculated interlayer *d*-spacings were determined as 0.33, 0.41, 0.17 and 0.27 nm, corresponding to the (223), (220), (412) and (535) planes of Fe_3O_4, consistent with the XRD results.

Chemical compositional analysis of the elements was performed using electron diffraction spectroscopy (EDS) to confirm the presence of iron and oxygen in the Fe_3O_4 nanopowders. EDS analysis of Fe_3O_4 and Mo (2, 4 and 6%) doped Fe_3O_4 was conducted to assess the actual ratios of the elemental compositions, as indicated in Fig. S4(a–d)†. The peaks confirm the existence of iron (Fe), oxygen (O), and molybdenum (Mo) in the host and doped samples. Moreover, the appearance of carbon (C), gold (Au) and silicon (Si) peaks can be ascribed to the experimental setup and sample preparation methods.[55] The samples were coated with gold to decrease charge effects, causing Au peaks to appear in the spectra. Cu peaks were
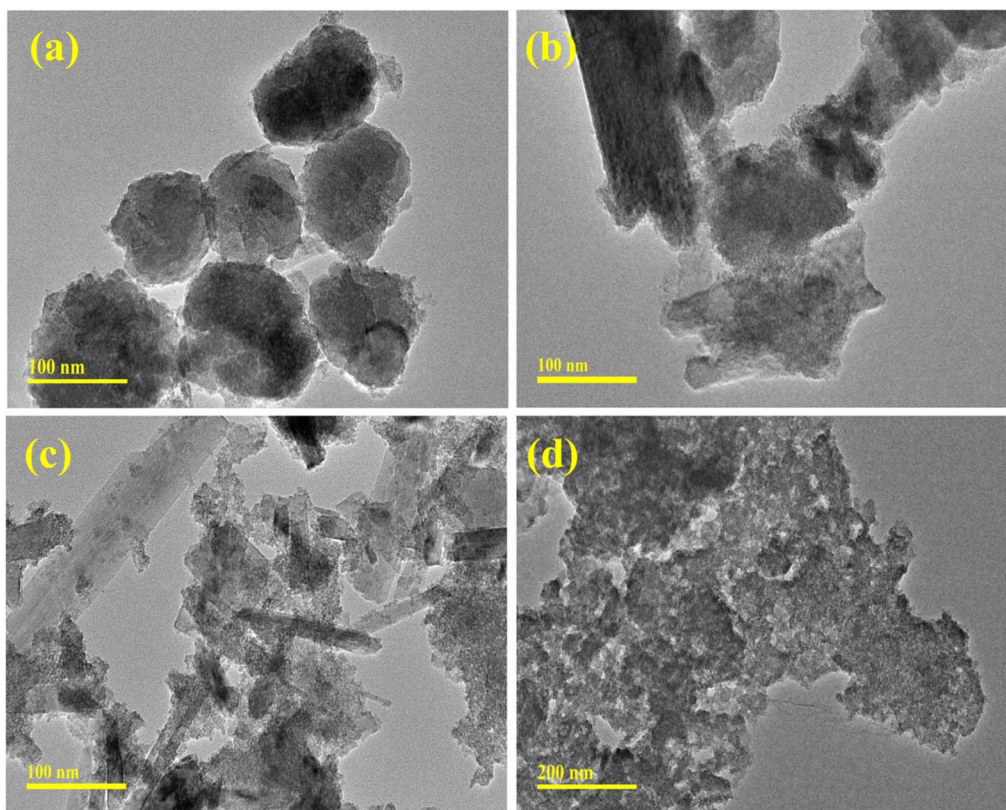
Fig. 3 TEM analysis of the (a) Fe_3O_4, (b) 2% $Mo-Fe_3O_4$, (c) 4% $Mo-Fe_3O_4$, and (d) 6% $Mo-Fe_3O_4$ samples.

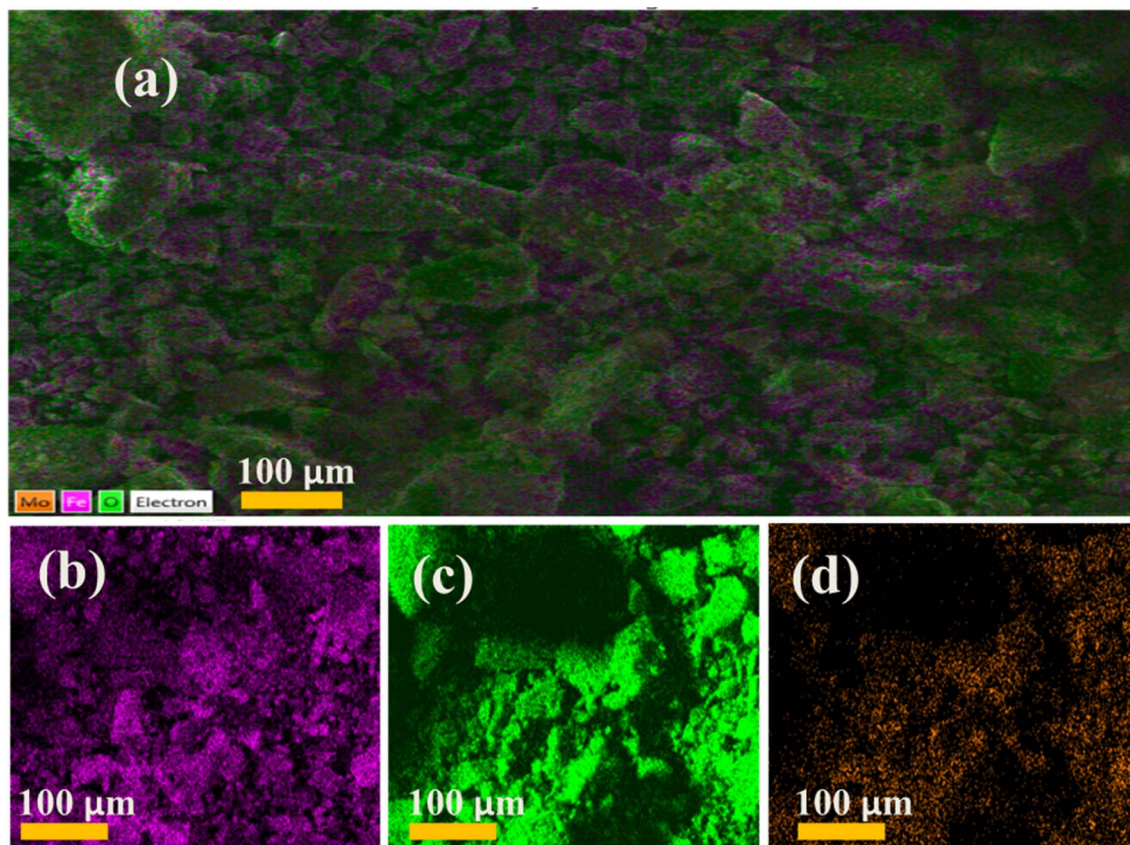**Fig. 4** The elemental mapping of the synthesized sample (a) Fe_3O_4, (b) 2% Mo, (c) 4% Mo, and (d) 6% $Mo-Fe_3O_4$.

a result of the Cu tape used in the sample holder. The Na peak can be attributed to NaOH used to preserve the precipitate and pH of the samples during their preparation. The elemental mapping images of pristine Fe_3O_4 and Mo-Fe_3O_4 at various concentrations of Mo are shown in Fig. 4a–d, indicating the clear appearance of Fe, O and Mo uniformly dispersed in the sample with a high amount of doped Mo.

UV-vis spectroscopy was performed to examine the optical characteristics of the synthesized samples in the range of 200–800 nm, with the results shown in Fig. 5a. The pronounced absorption peaks at 448 nm observed for the host sample correspond to a direct band-gap energy of around 2.7 eV.[29] The incorporation of Mo (various concentrations) in the host sample manifests in different energy levels that induce a red-shifting of the UV-vis bands. The energy band gap (E_g) of pristine and doped samples decreased from 2.76–2.64 eV upon increasing the concentration (2, 4 and 6%) of doping, as represented in Fig. 5b. The E_g of the Mo-doped Fe_3O_4 samples decreased as they absorb more photons than pristine Fe_3O_4, resulting in the generation of more electron–hole pairs.[56]

PL spectroscopy was executed to examine the photo-generated carrier trapping, charge transfer efficiency and recombination rate of the electron–hole pairs of the semiconductor material. PL spectra of Fe_3O_4 and Mo-Fe_3O_4 were recorded with a wide emission signal in the range of 360–410 nm, as revealed in Fig. 5c. The electron was excited to the conduction band (CB) at a wavelength of 250 nm, which resulted in the formation of a gaping hole in the material.[57] The recombination of charge carriers (e^- and h^+) in the excited state led to an emission at 390 nm. The valence band (VB) of Fe_3O_4 is composed of states of iron (3d) and oxygen (2p) that are both present in the compound and CB is made up of the Fe (4s) state. The graph shows a single high-intensity peak for the 2% Mo-Fe_3O_4 at 392 nm caused by the high charge recombination rate of electron–hole pairs, and with a higher concentration of doping this peak lowered in intensity, which in turn significantly boost the CA.[58] The higher intensity of the PL spectra manifested in a lower amount of surface oxygen vacancies and lower peak intensity, indicating higher catalytic activity, as suggested by previous studies.[59]

The catalytic degradation of dye was performed using the synthesized NSs *via* the electron transfer of BH_4^- ions. The catalytic reduction of MB in the presence of the reducing agent $NaBH_4$ by the pristine Fe_3O_4 and Mo-Fe_3O_4 NSs samples was monitored using UV-vis spectroscopy, with the results shown in Fig. 6a–c.

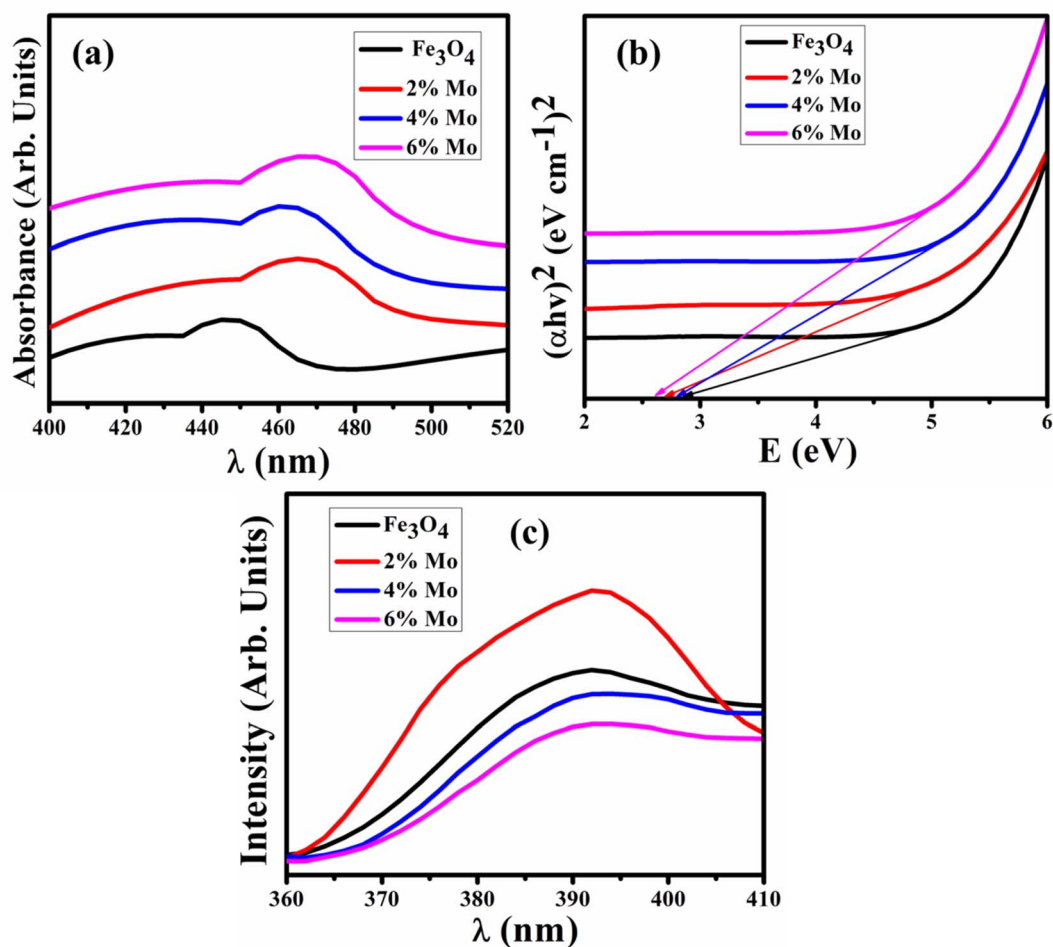**Fig. 5** (a) UV-vis spectra, (b) Tauc plot of E_g, and (c) PL spectra of the Fe_3O_4 and Mo-Fe_3O_4 samples.
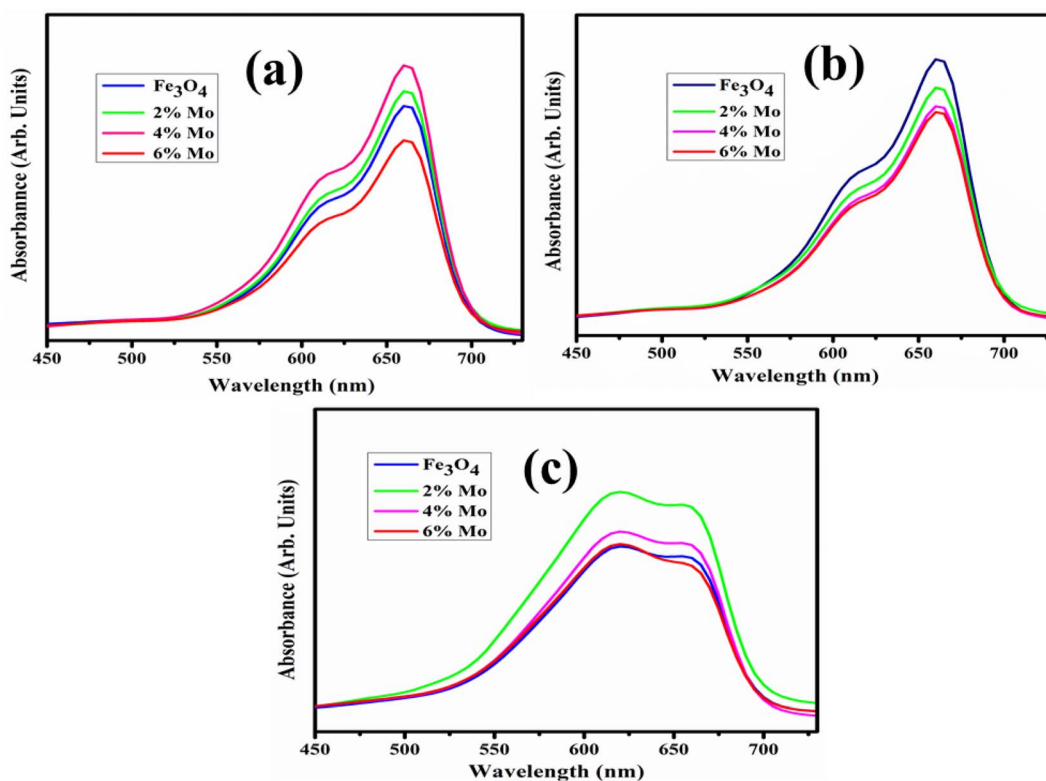
Fig. 6 (a–c) UV-vis spectra of dye reduction in (a) acidic, (b) neutral, and (c) basic media.

MB is a positively-charged dye that exhibits degradation upon incorporating BH_4^- ions that act as a reducing agent, decreasing the intensity of the absorption of dye molecules. The dye molecules accept the electrons contributed by the BH_4^- ions, resulting in the degradation of the MB dye. This promotes the catalytic degradation of MB, and active catalysts Fe_3O_4 NSs were selected as a framework to increase the efficiency of the dye degradation due to the unique properties that they possess such as easy magnetic separation, high specific surface area, a reactive surface and small size. The positively-charged MB dye forms hydrogen bonds with the hydroxyl groups (OH^-) located on the surface of the Fe_3O_4 NSs. This interaction is further strengthened by electrostatic attraction, which helps to facilitate MB dye adsorption. The surface-to-volume ratio was increased owing to the effect of the Fe_3O_4 NSs and the number of dye molecules, and BH_4^- ions could be effectively adsorbed. The adsorbed BH_4^- ions donate electrons to the surface of the Fe_3O_4 NSs. The MB dye interacts with the excess surface electrons of the electron-rich Fe_3O_4, leading to its degradation, as shown in Fig. S1.†

It has been observed that advanced oxidation processes are primarily affected by pH. As a result, it is critical to investigate the efficiency of catalysts to degrade dye at various pH levels in neutral acidic and basic media. The pH of a solution is an important factor in CA as it affects the surface characteristics of dye molecules and catalysts. The maximum degradation in each medium was assessed by the catalytic degradation of MB dye with the synthesized NSs catalysts. In neutral medium at pH =

7.4, 76.9, 78.3 and 79% degradation of MB was observed, at pH = 4 in acidic medium 73.26, 72, 68.7 and 77.63% degradation was observed, and in basic medium at pH = 12 maximum degradations of MB of 85.33, 81.48, 83.81, 86.25% were observed, respectively, as indicated in Fig. 7a–c. Because of its multiple roles, interpreting the influence that pH has on the catalytic degradation process is challenging. First, it is associated with the acid–base properties of the MO surface. The attachment of individual water molecules (H_2O) to surface metal sites is accompanied by OH^- charge group dissociation due to interaction with the chemically equivalent metal hydroxyl (M–OH) groups. As the pH of the solution continues to increase, the catalyst surface acquires a negative charge as the consequence of adsorbing OH^- ions. The availability of high amounts of OH^- ions on the particle surface and in the reaction system promotes the formation of ˙OH free radicals, which are broadly supported as the primary oxidizing species responsible for the degradation of organic compounds at neutral or high pH levels, increasing the process efficiency. The experimental analysis indicates that a higher level of degradation occurs in basic rather than acidic medium.[60] MB is a positively-charged dye with modest degradation at low pH. As the pH increased, maximum degradation was noted. The positively-charged surface of the catalyst is strongly opposed to cationic species adsorption in an acidic medium. Because of the increased electrostatic attraction between both the positively-charge dye and the negatively-charged catalyst in the basic medium, the surface charges of the dye become negative. Dye adsorption
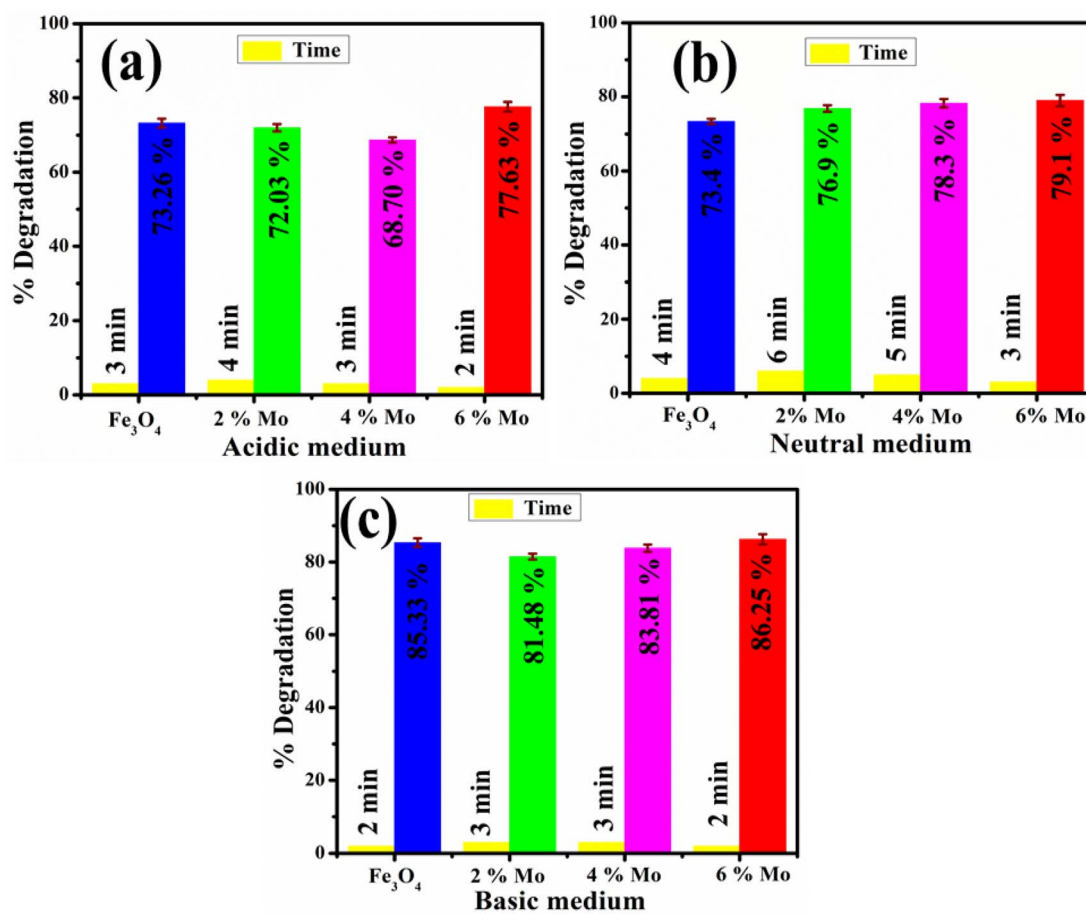
Fig. 7 Catalytic potential of the pristine and Mo-doped Fe_3O_4 in (a) acidic, (b) neutral, and (c) basic media.

increases as a result, which is consistent with previous findings.[61,62]

Using an agar well diffusion method, the antimicrobial performance of the host and Mo-doped Fe_3O_4 NSs against *E. coli* was assessed. The significant inhibition regions were measured at low and high concentrations (0–1.45 mm) and (1.65–3.45 mm), respectively, for *E. coli* and are presented in Table 1. In a comparable pattern, the inhibition zone quantification for *E. coli* was contrasted with a negative control, which consisted of DIW (0 mm), and positive control, which constituted

ciprofloxacin, with an inhibition zone measurement of 5.0 mm. Fe_3O_4 showed no inhibition zones during measurements when it was present in low concentrations, but it showed maximum inhibition zones when it was present in high concentrations. Additionally, as the dopant concentration was increased, the zone area also increased, as shown in Table 1. Because the cell wall of *E. coli* is primarily made up of an outer membrane, plasma membrane and a thin layer of peptidoglycan, the results showed that Mo-doped Fe_3O_4 NSs had a greater bactericidal efficiency against *E. coli*. Gram-negative microbes are distinguished from their Gram-positive counterparts by their cells' thicker cell walls and more intricate structures. NSs generate oxidative stress in proportion to their size, shape and concentration. Antibacterial activity is affected by particle concentration and size. When particles are smaller in size, they generate more reactive oxygen species, known as ROS. These species, in turn, cause cytoplasmic components to extrude, which ultimately results in the death of bacteria through microorganism membrane penetration,[63] as the mechanism of antimicrobial activity indicates in Fig. 8.

Pairs of electrons and holes are the fundamental basis for generating ROS. Chemical techniques yield more ROS, such as superoxide anion ($^\bullet O^{2-}$), hydrogen peroxide ($^\bullet H_2O_2$) and hydroxyl ($^\bullet OH$) radicals. Many oxides of transition metals are

Table 1 Antibacterial potential of Fe_3O_4 and Mo (2, 4 and 6%) doped Fe_3O_4

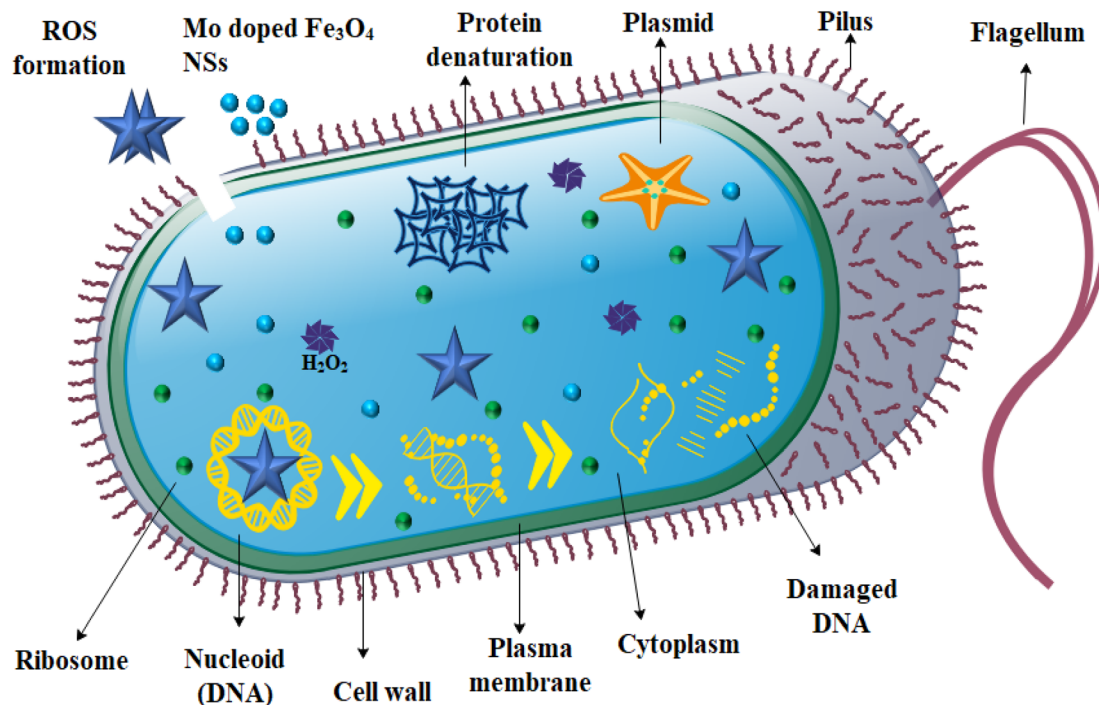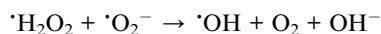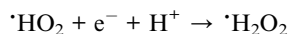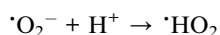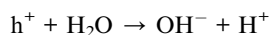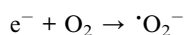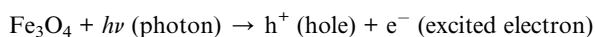|	*E. coli* inhibition zone measurements (mm)			
	Low conc.	High conc.	C +ve	C −ve
Samples	0.5 mg per 50 μL	1.0 mg per 50 μL	Ciprofloxacin	DIW
Fe_3O_4	0	1.65	5	0
2% Mo-Fe_3O_4	0	2.05	5	0
4% Mo-Fe_3O_4	0.65	2.45	5	0
6% Mo-Fe_3O_4	1.45	3.45	5	0

Fig. 8 Antimicrobial mechanism of the Mo-doped Fe_3O_4 NSs.

active in the comparison of a wide variety of microorganisms. This is because of the interaction between hydrophobic and electrostatic influences. The production of ROS can be described as follows.[64,65]

$$Fe_3O_4 + h\nu \text{ (photon)} \rightarrow h^+ \text{ (hole)} + e^- \text{ (excited electron)}$$

$$e^- + O_2 \rightarrow {}^{\cdot}O_2^-$$

$$h^+ + H_2O \rightarrow OH^- + H^+$$

$${}^{\cdot}O_2^- + H^+ \rightarrow {}^{\cdot}HO_2$$

$${}^{\cdot}HO_2 + e^- + H^+ \rightarrow {}^{\cdot}H_2O_2$$

$${}^{\cdot}H_2O_2 + {}^{\cdot}O_2^- \rightarrow {}^{\cdot}OH + O_2 + OH^-$$

When Fe_3O_4 and Mo-doped Fe_3O_4 are subjected to light irradiation with a photon energy equivalent to the E_g of the semiconductor material, charged particles from the VB at the lowest energy state are transferred to the CB, leaving holes in the VB. Excited electrons in the CB have the potential to become trapped by the molecular O_2 found on the surface, which results in the formation of superoxide anion radicals. As a result of this, the holes in the VB interact with H_2O, which results in the release of hydroxyl and hydrogen ions. The reaction between superoxide anion radicals and hydrogen ions then results in the production of hydroperoxyl radicals. The generation of the hydrogen peroxide radicals occurs as a result of hydroperoxyl radicals combining with electrons and holes. At the same time, hydroxyl radicals, hydroxyl ions, and singlet oxygen molecule

are generated when the hydrogen peroxide radicals combines with superoxide anion radicals. Positively-charged particles incorporating hydrogen peroxide radicals are capable of rapidly penetrating into bacterial cell (negatively charged) membranes, causing the death of bacteria, in contrast to negatively-charged radicals, which include hydroxyl radicals and superoxide anions, which are unable to pass through the cell membranes of microorganisms but still cause significant damage to the outermost surface of bacterial cells. Because of this, ${}^{\cdot}H_2O_2$ is extremely dangerous as it ruptures the cell membranes of bacteria, ultimately resulting in their death.[66] The bactericidal ability is related to the generation of ROS, which is influenced by a number of factors, including the ability to diffuse, crystallinity, surface area, and surface oxygen vacancies.[67]

NSs attach themselves to the cell wall like a helical, disorganized spring, and then they penetrate into the cell membrane, where they form interlinks with the molecular structure of deoxyribonucleic acid (DNA). Nanoparticles have a positive charge, in contrast to the membrane of the microbial species, which has a negative charge. The interaction between bacteria and a strong cationic (Fe^{3+}) charge increases microbicidal potency with increasing concentrations of NSs, which promotes lysis and bacterial cell collapse, ultimately leading to the death of bacteria.[63,68]

There is an ongoing need for suitable antibiotics, as drug resistance has been deemed a severe menace to mankind. The antibacterial action of metal NSs is widely recognized in this regard. The folate biosynthesis pathway enzymes dihydrofolate reductase (DHFR) and dihydropteroate synthase (DHPS) are well-known targets for trimethoprim and sulfonamide drugs.[69,70] Here, we assessed the affinity of Mo-Fe_3O_4 NSs for the

E. coli DHFR, DHPS, and FabH enzymes. Docked complexes indicated their binding pattern within active sites and asserted them as potential enzyme inhibitors towards certain enzyme targets. The optimally docked zone for DHFR$_{E. coli}$ displayed H-bonding interactions with Ile94, Ala7, and Asp27, with a binding score of -6.01 kcal mol^{-1}, as represented in Fig. 9e and f. In Fig. 9c and d, the docking complexes for DHPS$_{E. coli}$ exhibit H-bonding with Asn115, Asp56, Thr62, and Asp96.

These Mo-doped Fe$_3$O$_4$ NSs impede the DHPS enzyme's active site (binding energy: -6.17 kcal mol^{-1}) and are proposed as a potential antagonist. Docking of the Mo-doped Fe$_3$O$_4$ NSs with the β-ketoacyl-acyl carrier protein synthase III (FabH) enzyme of the fatty acid biosynthesis pathway displayed H-bonding interactions with Phe304, His244, and Asn274, with a binding score of 5.75 kcal mol^{-1}, as indicated in Fig. 9a and b. The inability of the substrate to enter the active site as a result of ligand binding
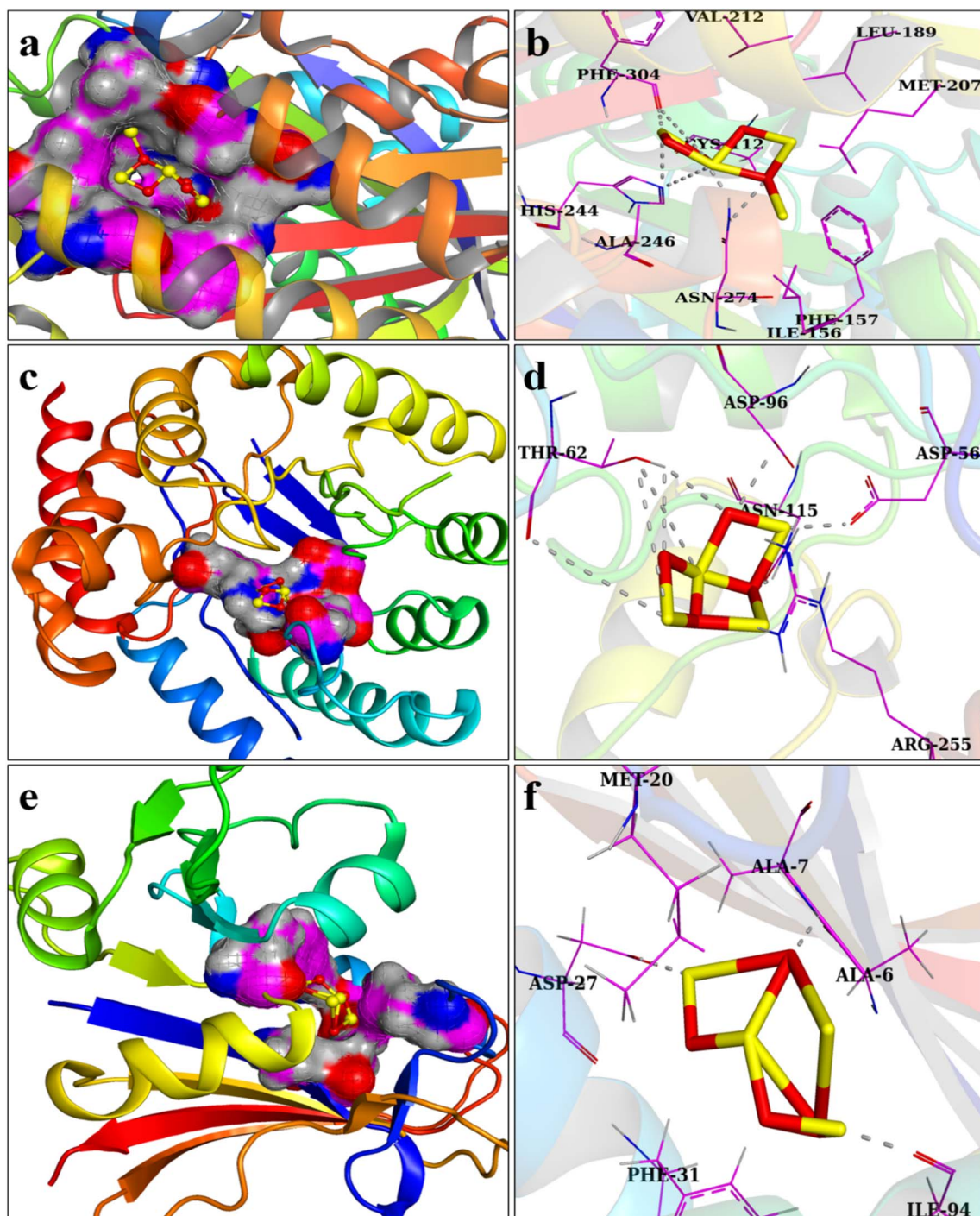
Fig. 9 Schematics of the binding pocket and interaction of Mo-doped Fe$_3$O$_4$ NSs inside (a, b) an active pocket of the β-ketoacyl-acyl carrier protein synthase III (FabH), (c, d) dihydropteroate synthase (DHPS), and (e, f) dihydrofolate reductase (DHFR) in *E. coli*.

led to cessation of the enzyme activity. Enhanced antibacterial activity of Mo-doped Fe_3O_4 NSs *versus E. coli in silico* predictions for specified targets indicated their potential binding modes in the active pocket and showed them to be a prospective enzyme inhibitor.

4 Conclusion

In this study, Fe_3O_4 and Mo-Fe_3O_4 (2, 4 and 6%) nanostructures were synthesized *via* a co-precipitation approach to achieve improved catalytic and bactericidal activity, with molecular docking analysis also carried out. The XRD analysis revealed that the orthorhombic and tetragonal structure phases of Fe_3O_4 and crystalline suppression upon doping. The measured crystallite sizes for pure and doped Fe_3O_4 are 36.11, 38.45, 25.74, and 24.38 nm, with the peaks at 2θ of 26.6, 26.6, 28.3 and 36.26 corresponding to the (223), (223), (031) and (517) planes, respectively. UV-vis spectra showed peaks at 448 nm with an energy band gap at around 2.7 eV, showing a red-shift upon the incorporation of Mo (2, 4 and 6%), which indicates a decrease in the band gap energy to 2.64 eV for 6% Mo-doped Fe_3O_4 NSs. The mapping analysis and EDS spectra demonstrated the elemental composition and presence of Fe and O, and the doping of Mo. Furthermore, TEM analysis showed agglomerated spherical-shaped nanoparticles in the pure sample, where upon the addition of a low concentration of Mo, agglomerated nanorods and nanoparticles were observed and with 6% incorporation of Mo surface floccules emerged on the surface of the nanoparticles. HR-TEM analysis was used to measure the interlayer *d*-spacing of the pure and doped samples, of 0.33, 0.41, 0.17 and 0.27 nm. Catalytic degradation of MB using $NaBH_4$ as a reducing agent was successful in acidic, neutral and basic media, with results of 77.63, 79.3 and 86.25%, respectively. 6% Mo-doped Fe_3O_4 was found to be the superior catalyst for the degradation of MB as a redox reaction take place between MB and $NaBH_4$. Antimicrobial activity measurements were conducted against *E. coli* bacteria and the results compared with ciprofloxacin. The significant inhibition zone for pure and doped samples was determined for high concentration as 1.65–3.45 mm. In addition, molecular docking analysis suggested that the Mo-doped Fe_3O_4 NSs might block the DHFR, DHPS, and FabH enzymes. The inhibition of certain enzymes has been proposed as a potential mechanism for the microbicidal effect of the Mo-doped Fe_3O_4 NSs toward *E. coli*. The experimental results indicate that the catalysts used in this study are efficient at eliminating toxic industrial effluents and infectious disease bacteria from wastewater, as well as being environmentally conscious, less noxious, and cost-effective compared with other systems, showing their future potential.

Conflicts of interest

The authors declare no conflict of interest.

Acknowledgements

References

1 R. Rajkumar, G. Ezhumalai and M. Gnanadesigan, A green approach for the synthesis of silver nanoparticles by Chlorella vulgaris and its application in photocatalytic dye degradation activity, *Environ. Technol. Innovation*, 2021, **21**, 101282, DOI: **10.1016/j.eti.2020.101282**.

2 M. M. Hasan, M. A. Shenashen, M. N. Hasan, H. Znad, M. S. Salman and M. R. Awual, Natural biodegradable polymeric bioadsorbents for efficient cationic dye encapsulation from wastewater, *J. Mol. Liq.*, 2021, **323**, 114587, DOI: **10.1016/j.molliq.2020.114587**.

3 A. Raza, M. Ikram, M. Aqeel, M. Imran, A. Ul-Hamid, K. N. Riaz and S. Ali, Enhanced industrial dye degradation using Co doped in chemically exfoliated MoS_2 nanosheets, *Appl. Nanosci.*, 2020, **10**, 1535–1544, DOI: **10.1007/s13204-019-01239-3**.

4 M. M. Ghangrekar and P. Chatterjee, Water pollutants classification and its effects on environment, in *Carbon Nanostructures*, Springer International Publishing, 2018, pp. 11–26, DOI: **10.1007/978-3-319-95603-9_2**.

5 R. N. Bharagava, G. Saxena and S. I. Mulla, Introduction to Industrial Wastes Containing Organic and Inorganic Pollutants and Bioremediation Approaches for Environmental Management, in *Bioremediation of Industrial Waste for Environmental Safety*, Springer Singapore, 2020, pp. 1–18, DOI: **10.1007/978-981-13-1891-7_1**.

6 J. bo Zhong, J. zhang Li, F. mei Feng, Y. Lu, J. Zeng, W. Hu and Z. Tang, Improved photocatalytic performance of SiO_2–TiO_2 prepared with the assistance of SDBS, *J. Mol. Catal. A: Chem.*, 2012, **357**, 101–105, DOI: **10.1016/j.molcata.2012.01.026**.

7 A. Ivanets, M. Roshchina, V. Srivastava, V. Prozorovich, T. Dontsova, S. Nahirniak, V. Pankov, A. Hosseini-Bandegharaei, H. Nguyen Tran and M. Sillanpää, Effect of metal ions adsorption on the efficiency of methylene blue degradation onto $MgFe_2O_4$ as Fenton-like catalysts, *Colloids Surf., A*, 2019, **571**, 17–26, DOI: **10.1016/j.colsurfa.2019.03.071**.

8 M. Gouamid, M. R. Ouahrani and M. B. Bensaci, Adsorption equilibrium, kinetics and thermodynamics of methylene blue from aqueous solutions using Date palm Leaves, *Energy Procedia*, 2013, 898–907, DOI: **10.1016/j.egypro.2013.07.103**.

9 F. Raposo, M. A. De La Rubia and R. Borja, Methylene blue number as useful indicator to evaluate the adsorptive capacity of granular activated carbon in batch mode: influence of adsorbate/adsorbent mass ratio and particle size, *J. Hazard. Mater.*, 2009, **165**, 291–299, DOI: **10.1016/j.jhazmat.2008.09.106**.

10 M. A. Haque, M. Shams-Ud-Din and A. Haque, The effect of aqueous extracted wheat bran on the baking quality of

biscuit, *Int. J. Food Sci. Technol.*, 2002, **37**, 453–462, DOI: 10.1046/j.1365-2621.2002.00583.x.

11 L. Spitaleri, G. Nicotra, M. Zimbone, A. Contino, G. Maccarrone, A. Alberti and A. Gulino, Fast and Efficient Sun Light Photocatalytic Activity of Au_ZnO Core-Shell Nanoparticles Prepared by a One-Pot Synthesis, *ACS Omega*, 2019, **4**, 15061–15066, DOI: 10.1021/acsomega.9b01850.

12 Z. Yuan, J. Wang, Y. Wang, Q. Liu, Y. Zhong, Y. Wang, L. Li, S. F. Lincoln and X. Guo, Preparation of a poly(acrylic acid) based hydrogel with fast adsorption rate and high adsorption capacity for the removal of cationic dyes, *RSC Adv.*, 2019, **9**, 21075–21085, DOI: 10.1039/c9ra03077h.

13 A. Lassoued, M. S. Lassoued, B. Dkhil, A. Gadri and S. Ammar, Structural, optical and morphological characterization of Cu-doped α-Fe$_2$O$_3$ nanoparticles synthesized through co-precipitation technique, *J. Mol. Struct.*, 2017, **1148**, 276–281, DOI: 10.1016/j.molstruc.2017.07.051.

14 H. Demissie, G. An, R. Jiao, T. Ritigala, S. Lu and D. Wang, Modification of high content nanocluster-based coagulation for rapid removal of dye from water and the mechanism, *Sep. Purif. Technol.*, 2021, **259**, 117845, DOI: 10.1016/j.seppur.2020.117845.

15 Q. Feng, B. Gao, Q. Yue and K. Guo, Flocculation performance of papermaking sludge-based flocculants in different dye wastewater treatment: comparison with commercial lignin and coagulants, *Chemosphere*, 2021, **262**, 128416, DOI: 10.1016/j.chemosphere.2020.128416.

16 H. Wu, X. Gao, M. Wu, Y. Zhu, R. Xiong and S. Ye, The efficiency and risk to groundwater of constructed wetland system for domestic sewage treatment – a case study in Xiangtan, China, *J. Cleaner Prod.*, 2020, **277**, 123384, DOI: 10.1016/j.jclepro.2020.123384.

17 H. Wu, J. Dai, S. Sun, C. Du, Y. Long, H. Chen, G. Yu, S. Ye and J. Chen, Responses of habitat suitability for migratory birds to increased water level during middle of dry season in the two largest freshwater lake wetlands of China, *Ecol. Indic.*, 2021, **121**, 107065, DOI: 10.1016/j.ecolind.2020.107065.

18 J. Fito, N. Tefera and S. W. H. Van Hulle, An Integrated Treatment Technology for Blended Wastewater of the Sugar Industry and Ethanol Distillery, *Environ. Processes*, 2019, **6**, 475–491, DOI: 10.1007/s40710-019-00366-x.

19 S. Ye, M. Yan, X. Tan, J. Liang, G. Zeng, H. Wu, B. Song, C. Zhou, Y. Yang and H. Wang, Facile assembled biochar-based nanocomposite with improved graphitization for efficient photocatalytic activity driven by visible light, *Appl. Catal., B*, 2019, **250**, 78–88, DOI: 10.1016/j.apcatb.2019.03.004.

20 S. Ye, W. Xiong, J. Liang, H. Yang, H. Wu, C. Zhou, L. Du, J. Guo, W. Wang, L. Xiang, G. Zeng and X. Tan, Refined regulation and nitrogen doping of biochar derived from ramie fiber by deep eutectic solvents (DESs) for catalytic persulfate activation toward non-radical organics degradation and disinfection, *J. Colloid Interface Sci.*, 2021, **601**, 544–555, DOI: 10.1016/j.jcis.2021.05.080.

21 J. Hassan, M. Ikram, A. Ul-Hamid, M. Imran, M. Aqeel and S. Ali, Application of Chemically Exfoliated Boron Nitride Nanosheets Doped with Co to Remove Organic Pollutants Rapidly from Textile Water, *Nanoscale Res. Lett.*, 2020, **15**, 75, DOI: 10.1186/s11671-020-03315-y.

22 A. Haider, M. Ijaz, S. Ali, J. Haider, M. Imran, H. Majeed, I. Shahzadi, M. M. Ali, J. A. Khan and M. Ikram, Green Synthesized Phytochemically (Zingiber officinale and Allium sativum) Reduced Nickel Oxide Nanoparticles Confirmed Bactericidal and Catalytic Potential, *Nanoscale Res. Lett.*, 2020, **15**, 50, DOI: 10.1186/s11671-020-3283-5.

23 M. Ali, M. Ikram, M. Ijaz, A. Ul-Hamid, M. Avais and A. A. Anjum, Green synthesis and evaluation of n-type ZnO nanoparticles doped with plant extract for use as alternative antibacterials, *Appl. Nanosci.*, 2020, **10**, 3787–3803, DOI: 10.1007/s13204-020-01451-6.

24 M. Á. Argudín, M. C. Mendoza and M. R. Rodicio, Food Poisoning and Staphylococcus aureus Enterotoxins, *Toxins*, 2010, **2**, 1751–1773, DOI: 10.3390/toxins2071751.

25 H. F. Chambers and F. R. DeLeo, Waves of resistance: Staphylococcus aureus in the antibiotic era, *Nat. Rev. Microbiol.*, 2009, **7**, 629–641, DOI: 10.1038/nrmicro2200.

26 J. M. Spinale, R. L. Ruebner, L. Copelovitch and B. S. Kaplan, Long-term outcomes of Shiga toxin hemolytic uremic syndrome, *Pediatr. Nephrol.*, 2013, **28**, 2097–2105, DOI: 10.1007/s00467-012-2383-6.

27 T. Abuladze, M. Li, M. Y. Menetrez, T. Dean, A. Senecal and A. Sulakvelidze, Bacteriophages reduce experimental contamination of hard surfaces, tomato, spinach, broccoli, and ground beef by Escherichia coli O$_{157}$:H$_7$, *Appl. Environ. Microbiol.*, 2008, **74**, 6230–6238, DOI: 10.1128/AEM.01465-08.

28 P. M. Hawkey, The growing burden of antimicrobial resistance, *J. Antimicrob. Chemother.*, 2008, **62**, i1–i9, DOI: 10.1093/jac/dkn241.

29 C. Siriwong, N. Wetchakun, B. Inceesungvorn, D. Channei, T. Samerjai and S. Phanichphant, Doped-metal oxide nanoparticles for use as photocatalysts, *Prog. Cryst. Growth Charact. Mater.*, 2012, **58**, 145–163, DOI: 10.1016/j.pcrysgrow.2012.02.004.

30 H. Li, H. Shen, L. Duan, R. Liu, Q. Li, Q. Zhang and X. Zhao, Enhanced photocatalytic activity and synthesis of ZnO nanorods/MoS$_2$ composites, *Superlattices Microstruct.*, 2018, **117**, 336–341, DOI: 10.1016/j.spmi.2018.03.028.

31 S. A. Ansari, M. M. Khan, M. O. Ansari, J. Lee and M. H. Cho, Biogenic synthesis, photocatalytic, and photoelectrochemical performance of Ag–ZnO nanocomposite, *J. Phys. Chem. C*, 2013, **117**, 27023–27030, DOI: 10.1021/jp410063p.

32 R. Ben Ayed, M. Ajili, Y. Piñeiro, J. Rivas and N. T. Kamoun, First investigation on (Ni, Co) co-doping effects on the physical properties of Fe$_2$O$_3$ thin films for optoelectronic applications, *Optik*, 2020, **213**, 164645, DOI: 10.1016/j.ijleo.2020.164645.

33 M. D. Nguyen, H. V. Tran, S. Xu and T. R. Lee, Fe$_3$O$_4$ nanoparticles: structures, synthesis, magnetic properties,

surface functionalization, and emerging applications, *Appl. Sci.*, 2021, **11**, 11301, DOI: **10.3390/app112311301**.

34 F. Yi, H. Gan, H. Jin, W. Zhao, K. Zhang, H. Jin, H. Zhang, Y. Qian and J. Ma, Sulfur- and chlorine-co-doped g-C$_3$N$_4$ nanosheets with enhanced active species generation for boosting visible-light photodegradation activity, *Sep. Purif. Technol.*, 2020, **233**, 115997, DOI: **10.1016/j.seppur.2019.115997**.

35 F. Yi, J. Liu, G. Liang, X. Xiao and H. Wang, Insight into the enhanced degradation mechanism of g-C$_3$N$_4$/g-C$_3$N$_5$ heterostructures through photocatalytic molecular oxygen activation in Van der Waals junction and excitation, *J. Alloys Compd.*, 2022, **905**, 164064, DOI: **10.1016/j.jallcom.2022.164064**.

36 J. G. Holt, N. R. Krieg, P. H. A. Sneath, J. T. Staley and S. T. Williams, *Bergey's Manual of determinate bacteriology*, 1994, **https://agris.fao.org/agris-search/search.do?recordID=XF2015028636**.

37 A. W. Bauer, W. M. Kirby, J. C. Sherris and M. Turck, Antibiotic susceptibility testing by a standardized single disk method, *Am. J. Clin. Pathol.*, 1966, **45**, 493–496, DOI: **10.1093/ajcp/45.4_ts.493**.

38 F. Adzitey, S. Yussif, R. Ayamga, S. Zuberu, F. Addy, G. Adu-Bonsu, N. Huda and R. Kobun, Antimicrobial Susceptibility and Molecular Characterization of *Escherichia coli* Recovered from Milk and Related Samples, *Microorganisms*, 2022, **10**, 1–13, DOI: **10.3390/microorganisms10071335**.

39 P. A. Wayne, Performance standards for antimicrobial susceptibility testing, *Clin. Lab. Stand. Inst. 24th Inter*, 2014.

40 B. A. Iwalokun, A. Ogunledun, D. O. Ogbolu, S. B. Bamiro and J. Jimi-Omojola, In vitro antimicrobial properties of aqueous garlic extract against multidrug-resistant bacteria and Candida species from Nigeria, *J. Med. Food*, 2004, **7**, 327–333, DOI: **10.1089/jmf.2004.7.327**.

41 A. Haider, M. Ijaz, M. Imran, M. Naz, H. Majeed, J. A. Khan, M. M. Ali and M. Ikram, Enhanced bactericidal action and dye degradation of spicy roots' extract-incorporated fine-tuned metal oxide nanoparticles, *Appl. Nanosci.*, 2020, **10**, 1095–1104, DOI: **10.1007/s13204-019-01188-x**.

42 R. L. Summerfield, D. M. Daigle, S. Mayer, D. Mallik, D. W. Hughes, S. G. Jackson, M. Sulek, M. G. Organ, E. D. Brown and M. S. Junop, A 2.13 Å structure of *E. coli* dihydrofolate reductase bound to a novel competitive inhibitor reveals a new binding surface involving the M$_{20}$ loop region, *J. Med. Chem.*, 2006, **49**, 6977–6986, DOI: **10.1021/jm060570v**.

43 M. L. Dennis, M. D. Lee, J. R. Harjani, M. Ahmed, A. J. DeBono, N. P. Pitcher, Z. C. Wang, S. Chhabra, N. Barlow, R. Rahmani, B. Cleary, O. Dolezal, M. Hattarki, L. Aurelio, J. Shonberg, B. Graham, T. S. Peat, J. B. Baell and J. D. Swarbrick, 8-Mercaptoguanine Derivatives as Inhibitors of Dihydropteroate Synthase, *Chem.–Eur. J.*, 2018, **24**, 1922–1930, DOI: **10.1002/chem.201704730**.

44 D. C. McKinney, C. J. Eyermann, R. F. Gu, J. Hu, S. L. Kazmirski, S. D. Lahiri, A. R. McKenzie, A. B. Shapiro and G. Breault, Antibacterial FabH Inhibitors with Mode of Action Validated in Haemophilus influenzae by *in Vitro*

45 I. Shahzadi, M. Islam, H. Saeed, A. Haider, A. Shahzadi, J. Haider, N. Ahmed, A. Ul-Hamid, W. Nabgan, M. Ikram and H. A. Rathore, Formation of biocompatible MgO/cellulose grafted hydrogel for efficient bactericidal and controlled release of doxorubicin, *Int. J. Biol. Macromol.*, 2022, **220**, 1277–1286, DOI: **10.1016/j.ijbiomac.2022.08.142**.

46 M. Ikram, K. Chaudhary, A. Shahzadi, A. Haider, I. Shahzadi, A. Ul-Hamid, N. Abid, J. Haider, W. Nabgan and A. R. Butt, Chitosan/Starch-doped MnO$_2$ nanocomposite served as dye degradation, bacterial activity and insilico molecular docking study, *Mater. Today Nano*, 2022, 100271, DOI: **10.1016/j.mtnano.2022.100271**.

47 J. Xiao, B. Du, S. Hu, J. Zhong, X. Chen, Y. Zhang, D. Cai, S. F. Zhou and G. Zhan, Simultaneously Enhanced Charge Separation and Transfer in Cocatalyst-Free Hematite Photoanode by Mo/Sn Codoping, *ACS Appl. Energy Mater.*, 2021, **4**, 10368–10379, DOI: **10.1021/acsaem.1c02291**.

48 F. Soflaee, M. Farahmandjou and T. P. Firoozabadi, Polymer-mediated synthesis of iron oxide (Fe$_2$O$_3$) nanorod, *Chin. J. Phys.*, 2015, **53**, DOI: **10.6122/CJP.20150413**.

49 T. W. Sun, Y. J. Zhu, C. Qi, G. J. Ding, F. Chen and J. Wu, α-Fe$_2$O$_3$ nanosheet-assembled hierarchical hollow mesoporous microspheres: microwave-assisted solvothermal synthesis and application in photocatalysis, *J. Colloid Interface Sci.*, 2016, **463**, 107–117, DOI: **10.1016/j.jcis.2015.10.038**.

50 M. Mohapatra, S. Layek, S. Anand, H. C. Verma and B. K. Mishra, Structural and magnetic properties of Mg-doped nano-α-Fe$_2$O$_3$ particles synthesized by surfactant mediation-precipitation technique, *Phys. Status Solidi B Basic Res.*, 2013, **250**, 65–72, DOI: **10.1002/pssb.201248151**.

51 P. A. Sundaram, R. Augustine and M. Kannan, Extracellular biosynthesis of iron oxide nanoparticles by *Bacillus subtilis* strains isolated from rhizosphere soil, *Biotechnol. Bioprocess Eng.*, 2012, **17**, 835–840, DOI: **10.1007/s12257-011-0582-9**.

52 M. Yadav, Study on thermal and mechanical properties of cellulose/iron oxide bionanocomposites film, *Compos. Commun.*, 2018, **10**, 1–5, DOI: **10.1016/j.coco.2018.04.010**.

53 G. Chizari Fard, M. Mirjalili and F. Najafi, Hydroxylated α-Fe$_2$O$_3$ nanofiber: optimization of synthesis conditions, anionic dyes adsorption kinetic, isotherm and error analysis, *J. Taiwan Inst. Chem. Eng.*, 2017, **70**, 188–199, DOI: **10.1016/j.jtice.2016.10.045**.

54 Z. Lu, J. Dai, X. Song, G. Wang and W. Yang, Facile synthesis of Fe$_3$O$_4$/SiO$_2$ composite nanoparticles from primary silica particles, *Colloids Surf., A*, 2008, **317**, 450–456, DOI: **10.1016/j.colsurfa.2007.11.020**.

55 A. D. Khan, M. Ikram, A. Haider, A. Ul-Hamid, W. Nabgan and J. Haider, Polyvinylpyrrolidone and chitosan-doped lanthanum oxide nanostructures used as anti-bacterial agents and nano-catalyst, *Appl. Nanosci.*, 2022, **12**, 2227–2239, DOI: **10.1007/s13204-022-02471-0**.

56 Z. Masoumi, M. Tayebi and B. K. Lee, The role of doping molybdenum (Mo) and back-front side illumination in

Resistance Mutation Mapping, *ACS Infect. Dis.*, 2016, **2**, 456–464, DOI: **10.1021/acsinfecdis.6b00053**.

enhancing the charge separation of α-Fe₂O₃ nanorod photoanode for solar water splitting, *Sol. Energy*, 2020, **205**, 126–134, DOI: **10.1016/j.solener.2020.05.044**.

57 A. Lassoued, M. S. Lassoued, B. Dkhil, S. Ammar and A. Gadri, Synthesis, photoluminescence and Magnetic properties of iron oxide (α-Fe₂O₃) nanoparticles through precipitation or hydrothermal methods, *Phys. E*, 2018, **101**, 212–219, DOI: **10.1016/j.physe.2018.04.009**.

58 G. Nabiyouni and D. Ghanbari, Thermal, magnetic, and optical characteristics of ABS-Fe 2O 3 nanocomposites, *J. Appl. Polym. Sci.*, 2012, **125**, 3268–3274, DOI: **10.1002/app.36514**.

59 X. Li, S. Li, H. Hu, T. Sun and S. Yang, Facet Effects of α-Fe₂O₃ with Different Morphologies on the Thermal Decomposition of Ammonium Erchlorate, *Catal. Lett.*, 2022, **152**(11), 1–10, DOI: **10.1007/s10562-021-03902-3**.

60 A. Krishnan, P. V. Vishwanathan, A. C. Mohan, R. Panchami, S. Viswanath and A. V. Krishnan, Tuning of Photocatalytic Performance of CeO₂-Fe₂O₃ Composite by Sn-doping for the Effective Degradation of Methylene Blue (MB) and Methyl Orange (MO) dyes, *Surf. Interfaces*, 2021, **22**, 100808, DOI: **10.1016/j.surfin.2020.100808**.

61 M. Ikram, T. Inayat, A. Haider, A. Ul-Hamid, J. Haider, W. Nabgan, A. Saeed, A. Shahbaz, S. Hayat, K. Ul-Ain and A. R. Butt, Graphene Oxide-Doped MgO Nanostructures for Highly Efficient Dye Degradation and Bactericidal Action, *Nanoscale Res. Lett.*, 2021, **16**, 56, DOI: **10.1186/s11671-021-03516-z**.

62 M. Ikram, N. Abid, A. Haider, A. Ul-Hamid, J. Haider, A. Shahzadi, W. Nabgan, S. Goumri-Said, A. R. Butt and M. Benali Kanoun, Toward efficient dye degradation and the bactericidal behavior of Mo-doped La₂O₃ nanostructures, *Nanoscale Adv.*, 2022, **4**, 926–942, DOI: **10.1039/d1na00802a**.

63 M. Mustajab, M. Ikram, A. Haider, A. Ul-Hamid, W. Nabgan, J. Haider, R. Ghaffar, A. Shahzadi, A. Ghaffar and A. Saeed, Promising performance of polyvinylpyrrolidone-doped bismuth oxyiodide quantum dots for antibacterial and

catalytic applications, *Appl. Nanosci.*, 2022, **12**, 2621–2633, DOI: **10.1007/s13204-022-02547-x**.

64 Z. N. Kayani, M. Sahar, S. Riaz, S. Naseem and Z. Saddiqe, Enhanced magnetic, antibacterial and optical properties of Sm doped ZnO thin films: role of Sm doping, *Opt. Mater.*, 2020, **108**, 110457, DOI: **10.1016/j.optmat.2020.110457**.

65 N. Rajiv Chandar, S. Agilan, R. Thangarasu, N. Muthukumarasamy, J. Chandrasekaran, S. Arunachalam and S. R. Akshaya, Elucidation of efficient dual performance in photodegradation and antibacterial activity by a promising candidate Ni-doped MoO₃ nanostructure, *J. Sol-Gel Sci. Technol.*, 2021, **100**, 451–465, DOI: **10.1007/s10971-020-05382-0**.

66 M. Ikram, A. Haider, M. Imran, J. Haider, S. Naz, A. Ul-Hamid, W. Nabgan, M. Mustajab, A. Shahzadi, I. Shahzadi, M. A. Raza and G. Nazir, Facile synthesis of starch and tellurium doped SrO nanocomposite for catalytic and antibacterial potential: *in silico* molecular docking studies, *Int. J. Biol. Macromol.*, 2022, **221**, 496–507, DOI: **10.1016/j.ijbiomac.2022.09.034**.

67 K. Karthik, S. Dhanuskodi, C. Gobinath, S. Prabukumar and S. Sivaramakrishnan, Fabrication of MgO nanostructures and its efficient photocatalytic, antibacterial and anticancer performance, *J. Photochem. Photobiol., B*, 2019, **190**, 8–20, DOI: **10.1016/j.jphotobiol.2018.11.001**.

68 K. Kannan, D. Radhika, A. S. Nesaraj, K. Kumar Sadasivuni, K. R. Reddy, D. Kasai and A. V Raghu, Photocatalytic, antibacterial and electrochemical properties of novel rare earth metal oxides-based nanohybrids, *Mater. Sci. Energy Technol.*, 2020, **3**, 853–861, DOI: **10.1016/j.mset.2020.10.008**.

69 M. Ikram, S. Abbasi, A. Haider, S. Naz, A. Ul-Hamid, M. Imran, J. Haider and A. Ghaffar, Bimetallic Ag/Cu incorporated into chemically exfoliated MoS₂ nanosheets to enhance its antibacterial potential: *in silico* molecular docking studies, *Nanotechnology*, 2020, **31**, 13, DOI: **10.1088/1361-6528/ab8087**.

70 S. Hawser, S. Lociuro and K. Islam, Dihydrofolate reductase inhibitors as antibacterial agents, *Biochem. Pharmacol.*, 2006, **71**, 941–948, DOI: **10.1016/j.bcp.2005.10.052**.